THE GEOLOGICAL SOCIETY OF AMERICA®

Open Access Article

Need for a Multi-Sensor Monitoring Approach for Embankment Failures: Lessons Learned from the Edenville Dam Failure

JOBIN THOMAS

Department of Geology and Geological Engineering, University of Mississippi, Oxford, MS 38677, USA

RYAN KLIDA

Department of Geological and Mining Engineering and Sciences, Michigan Technological University, Houghton, MI 49931, USA

THOMAS OOMMEN*

Department of Geology and Geological Engineering, University of Mississippi, Oxford, MS 38677, USA

SAJINKUMAR K.S.

Department of Geology, University of Kerala, Thiruvananthapuram, Kerala 695581, India

BIN ZHANG

Faculty of Geo-Information Science and Earth Observation, University of Twente, 7511 AE Enschede, The Netherlands

XIE HU

College of Urban and Environmental Sciences, Peking University, Beijing 100871, China

Key Terms: ***Embankment Failure, Edenville Dam, Synthetic Aperture Radar, Persistent Scatterer Interferometry, Soil Moisture Index***

ABSTRACT

The Edenville Dam, an earthen embankment in Midland, MI, failed on May 19, 2020, after 3 days of elevated rainfall (3.83–8.0 in.; 9.7–20 cm), which caused flooding downstream of the dam. Dam infrastructure similar to that at the Edenville Dam is not uncommon in the United States and hence requires periodic monitoring. A pre-failure analysis was conducted in the dam to explore the application of remote sensing in dam monitoring. Persistent scatterer interferometry (PSI), a form of synthetic aperture radar (SAR) interferometry, was used to analyze 97 Sentinel-1 images to measure the line-of-sight (LOS) displacement prior to the failure. The PSI analysis showed hardly any signs of deformation at the failure location and implied stable embankments with velocities ranging from 3.1 to −5.4 mm/yr. The soil moisture index (SMI) derived using 14 Landsat-8 images between 2016 and 2020 suggested the presence of subsurface seepage and a potential failure zone. This study illustrates the requirement for multi-sensor remote sensing–based approaches for continuous dam monitoring and analysis.

INTRODUCTION

On May 19, 2020, the Edenville Dam in Michigan, midwestern United States, failed due to static liquefaction instability after a heavy spell of rainfall spatially ranging between 3.83 in. (9.7 cm) and 8.0 in. (20 cm) over 2 days. The Edenville Dam, constructed between 1923 and 1925, was designed for flood control and hydroelectric power generation (Pradel et al., 2021; France et al., 2022). The failure resulted in the water impounded by the dam (Wixom Lake) surging downstream into Sanford Lake, ultimately leading to the overtopping and failure of

*Corresponding author email: toommen@olemiss.edu

the Sanford Dam on May 20, 2020. These events resulted in the inundation of the floodplains of the Tittabawassee and Tobacco Rivers, including the city of Midland, MI. The flood triggered the evacuation of 11,000 residents and caused an estimated 245 million U.S. dollars in property and infrastructure damages (Pradel et al., 2021; FEMA, 2022). Unfortunately, dam failures such as these are not uncommon in the United States (Graham, 2009). The Committee on Failures and Accidents to Large Dams of the U.S. Committee on Large Dams reported that natural erodible materials form the embankments for nearly 80 percent of the large dams in the United States (Redlinger et al., 1975). These structures are highly likely to be subject to deformation and failure, particularly under extreme hydrological conditions (Wu et al., 2011).

On a mean basis, roughly 10 dam failures occurred in the United States annually between 1848 and 2017, and recent decades show an increase in the number of failures (i.e., 24 per year) (National Performance of Dams Program, 2018). Years of neglecting aging infrastructure have left many dams in the United States in fair to poor conditions. According to the online dam inventory of the Dam Safety Program of the Michigan Department of Environment, Great Lakes and Energy (EGLE), Michigan has 2,545 dams with varying dimensions, where 10 percent of all the dams have "high" or "significant" hazard potential, including the Edenville and Sanford Dams before their failures (EGLE, 2023). The Michigan Section of the American Society of Civil Engineers (ASCE) (2023) listed dams in Michigan with an overall evaluation of a "C−" in their 2023 infrastructure report card, and at the time of the report, two thirds of the dams were older than their 50 year design life. Constructed in 1924, the Edenville Dam was designed before the modern geotechnical engineering practices of Professor Karl Terzaghi were widely practiced and built before the quality-control assessment of earth fill compaction was developed by Ralph Proctor in the 1930s (Pradel et al., 2021). Investigating the dam failure, the Embankments, Dams, and Slopes Committee of ASCE's Geo-Institute postulated possible failure mechanisms, including: (1) static liquefaction due to the rise in reservoir water elevation, resulting in loss of strength, and (2) slope instability due to the corresponding increased pore-water pressures (Pradel et al., 2021).

Dam embankments are subject to deformation and potential failure, mostly linked to inadequate design and/or construction, operational flaws, and high-magnitude floods (Foster et al., 2000; Graham, 2009). Such failures pose significant flood and debris risks to people, property, and infrastructure downstream of the structure. For instance, on October 4, 2010, the embankment failure of the No. 10 red mud reservoir in Hungary caused 10 fatalities and substantial economic losses (Grenerczy and Wegmüller, 2011). Similarly, the Fundão Dam in Brazil collapsed on November 5, 2015, killing 19 people and spilling about 32.6 million cubic meters of mining waste, causing severe environmental issues (Mura et al., 2018). In January 2019, the tailings dam of the Brumadinho iron mine in Brazil failed, resulting in a death toll of more than 250 (Silva Rotta et al., 2020). Had the instability of these embankments been detected at an early stage, appropriate measures could have been taken to prevent structural failure. Indeed, periodic embankment monitoring is a critical component in preventing the impacts of such unforeseen events. Furthermore, aging dam infrastructure increases the need for periodic dam inspections and monitoring to mitigate the risks associated with dam failures. Nevertheless, dam safety hugely relies on advancements in dam monitoring techniques.

Traditional dam inspection and monitoring methods require significant time and human resources in the field, and the monitoring data sets, such as global positioning system (GPS) data, elevation, and piezometer readings, offer only point information. On the other hand, remotely sensed data offer the ability to supplement *in situ* monitoring or replace *in situ*/field measurements where they are absent. Remote sensing can: (1) acquire continuous data over the entire embankment (as opposed to discrete, point-source data from *in situ* methods), (2) assess the structural condition and precursors of structural failures in a non-invasive manner, preventing any potential negative impact on the structure, and (3) continuously monitor the dam with minimal human resources. Interferometric synthetic aperture radar (InSAR) techniques are widely applied for monitoring earthen dam stability, where multi-temporal analysis of the synthetic aperture radar (SAR) images facilitates accurate monitoring of structural deformation. One of the robust methods is persistent scatterer interferometry (PSI), which uses permanent/persistent scatterers (PS) with high phase stability over long time intervals (Ferretti et al., 2001, 2011). However, the performance of PSI significantly depends on numerous factors, such as the sensor, number of SAR images, PS density, and deformation characteristics (Crosetto et al., 2016). Numerous researchers have demonstrated the applicability and competency of various InSAR-based approaches for monitoring the deformation of embankments and subsidence worldwide (e.g., Grenerczy and Wegmüller, 2011; Zhang et al., 2015; Othman et al., 2019; Besoya et al., 2020; and Maltese et al., 2021).

One of the major causes of earthen embankment failures is uncontrolled saturation and increased seepage due to internal erosion. Many researchers have illustrated the significance of various non-invasive monitoring methods to assess the structural hydrological condition, particularly based on remote-sensing data (Silva Rotta et al., 2020; Zumr et al., 2020; and Lin et al., 2021). Among the various approaches, the studies of Silva Rotta et al. (2020) and Lin et al. (2021) combined soil moisture

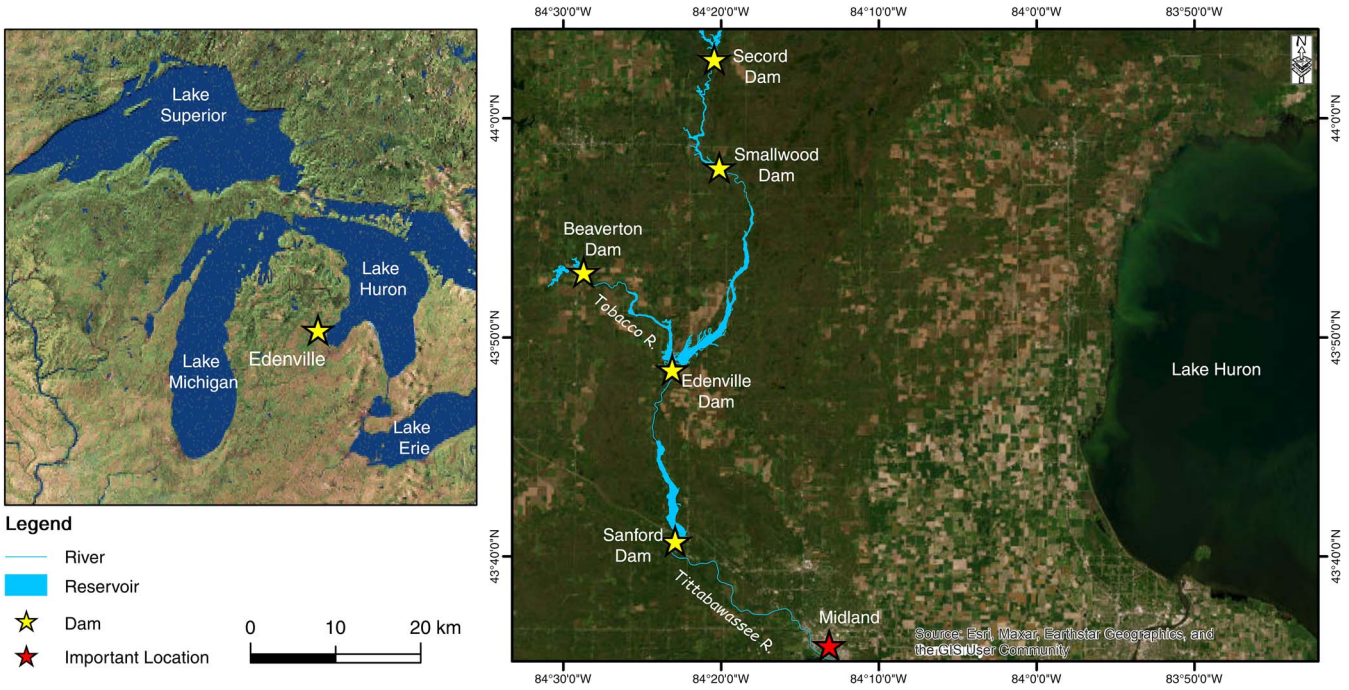

Figure 1. (a) Location of Edenville Dam in Michigan's Lower Peninsula. (b) Location of the five dams located along the Tittabawassee and Tobacco Rivers. Edenville Dam is located upstream of the confluence of the two rivers and impounds both rivers.

analysis using thermal and optical imagery with SAR analysis. The primary cause of the failure of the Brumadinho tailings dam was seepage erosion (piping), which was evident in the temporal variability of the soil moisture index (SMI) in the years prior to failure (Silva Rotta et al., 2020). Similarly, Lin et al. (2021), while analyzing the SMI time series between 2013 and 2020, noted a decadal increase in soil moisture along the eastern part of the collapsed area. Considering the applicability of SAR techniques and multi-spectral imaging for deformation studies, in this study, we utilized PSI and SMI to conduct a pre-failure analysis of the Edenville Dam.

THE EDENVILLE DAM: BACKGROUND

The Edenville Dam (Figure 1) is one of five dams along the Tittabawassee and Tobacco Rivers in the central region of Michigan's Lower Peninsula. Located along the border of Gladwin and Midland Counties, the Edenville Dam impounds the Tittabawassee and Tobacco Rivers just north of their confluence. The Tobacco River flows into the Tittabawassee River, downstream of the Edenville Dam and upstream of the Sanford Dam. The Edenville Dam consists of a series of earthen embankments, spillways, and a powerhouse spanning approximately 6,600 ft (2,012 m) across the Tittabawassee and Tobacco Rivers. The reservoir impounded by the dam is Wixom Lake. Figure 2 illustrates the geographical layout of Edenville Dam.

The Tobacco section is comprised of the Tobacco Spillway, the west embankment, and the west crest. The west embankment is approximately 1,300 ft (396 m) long and begins west of Michigan Highway M-30, extends westward to the Tobacco Spillway, and then continues to the west crest. The west crest is approximately 900 ft (274 m) long and extends west-northwest from the west embankment to the west abutment. The portion of the west embankment that lies west of the Tobacco Spillway and the west crest is a continuous embankment. However, they were separated in this study due to varying embankment heights. The west embankment has a height ranging from 32 to 47 ft (9.8 to 14.3 m), while the west crest has an approximate height of 12 ft (3.7 m). The upstream and downstream slopes of the embankments were initially constructed at a ratio of 2.5H:1V (horizontal to vertical) and 2H:1V, respectively (France et al., 2022). Portions of the downstream embankment slope have been flattened, and berms have been added. Survey data indicate that portions of the downstream slopes are steeper than the design ratio.

The Tittabawassee section is comprised of the southeast embankment, east embankment, and east crest. The southeast embankment begins south of the Edenville Spillway and extends southeast, approximately 650 ft (198 m) to the east abutment. The height of the southeast embankment ranged between 52 ft (15.8 m) immediately south of the spillway to 30 ft (9.1 m) toward the abutment. The approximate failure location is shown in Figure 2, and the height of the failure location was between 30 and 32 ft (9.1 and 9.8 m) (France et al., 2022). The

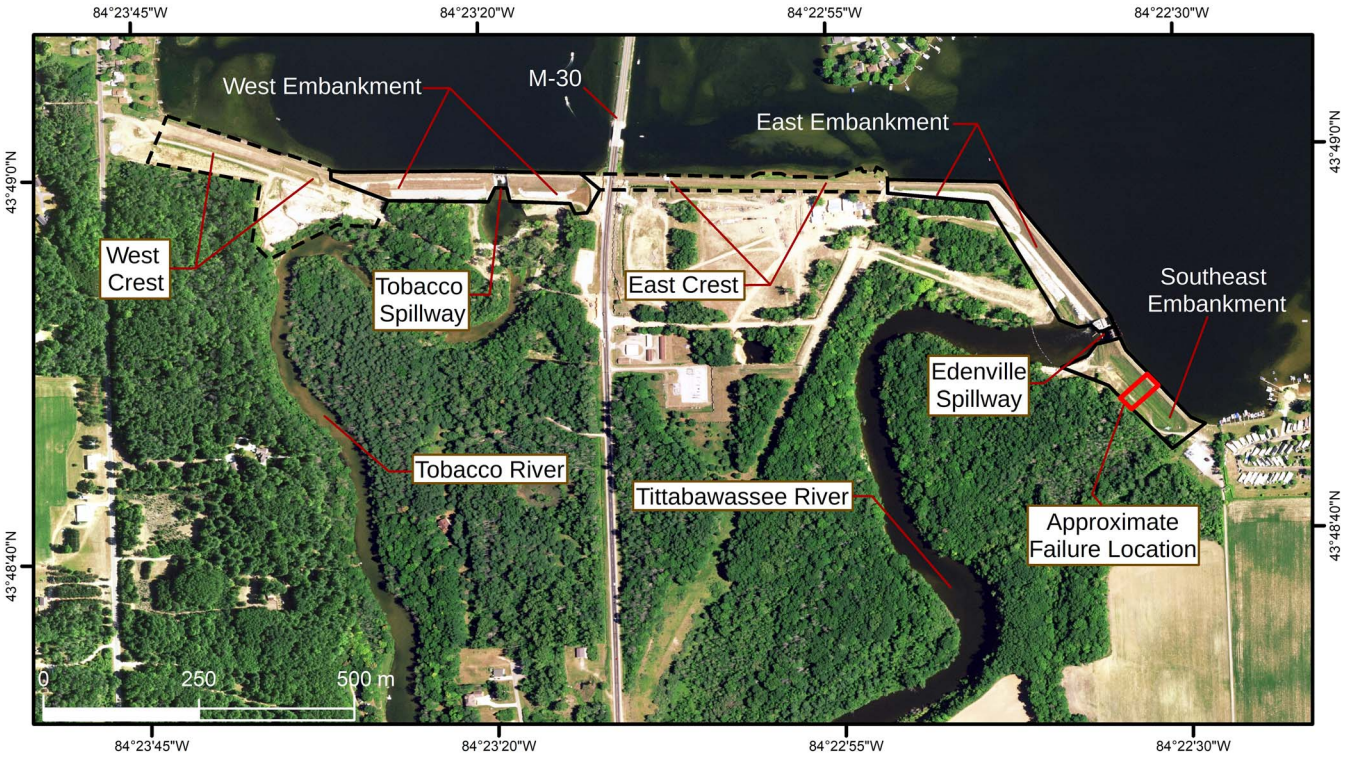

Figure 2. Edenville Dam site layout image. Highway M-30, shown in the center of the image, divides the dam into the Tobacco (western) and Tittabawassee (eastern) sections. (Background aerial image is courtesy of National Agriculture Imagery Program [NAIP], image captured on July 16, 2016 and accessed from the U.S. Geological Survey [USGS] Earth Explorer website: https://earthexplorer.usgs.gov.) The approximate failure location is shown in red.

east embankment and east crest are continuous embankments, but they were again separated in this study due to varying embankment heights. The east embankment extends from the Edenville Spillway 1,300 ft (396 m) to the east crest. The east crest extends 1,450 ft (442 m) from the east embankment to M-30. The average heights of the east embankment and east crest are 40 and 15 ft (12.2 and 4.6 m), respectively. Similar to the Tobacco section, the upstream and downstream slopes of the embankments were originally constructed at a ratio of 2.5H:1V (horizontal to vertical) and 2H:1V, respectively (France et al., 2022). Surveys conducted after the flood show that some sections of both the upstream and downstream embankments are steeper than the initial design ratio (France et al., 2022).

The Edenville Dam was built between 1923 and 1925 to manage flood waters and generate hydroelectric power (Pradel et al., 2021; France et al., 2022). The dam had two operating levels of the reservoir, normal and winter pool levels. The normal pool elevation was 675.8 ft (205.98 m), and the winter pool level was 672.8 ft (205.07 m) (Pradel et al., 2021). Daily variation in pool elevation was not to exceed 0.9 ft and 0.7 ft (0.27 and 0.21 m) for the normal and winter pools, respectively. The dam was constructed of loose, poorly graded sand without a clay core. The only sub-drain system consisted of clay drain tiles with outflows to a drainage ditch, which ran parallel to the toe of the embankment. According to historical photographs, fill was placed *en masse* rather than in lifts used in modern earth constructions. Fill was dumped via train car, and compaction efforts on the placed fill (i.e., rollers) were not recorded in the historical documentation (Pradel et al., 2021; France et al., 2022). The dam foundation consisted of glacial till and outwash sands, which were deposited during the retreat of the Saginaw Lobe of the Laurentide Ice Sheet. Post-glacial erosion and deposition produced a series of fluvial terraces along the Tittabawassee and Tobacco Rivers (Dorr and Eschman, 1970; Larson and Schaetzl, 2001; and Kehew et al., 2012). The variation in the elevation of the foundation terraces resulted in variation in the dam fill thickness throughout the structure.

The Edenville Dam failed on May 19, 2020, at approximately 5:30 pm EST after a 3 day elevated rainfall event. A total of 9.7 cm of rainfall was recorded for May 17–19 at the Edenville Dam (Pradel et al., 2021). On May 18, both spillways were operating at maximum capacity. A depression along the crest of the southeast embankment, at the approximate failure location shown in Figure 2, was noted by residents and bystanders about 30 minutes before failure. At the time of failure, it was estimated that the Wixom Lake reservoir elevation was

Figure 3. (a) Pre-failure and (b) post-failure imagery of the Edenville Dam. The approximate failure location where the depression was observed is shown in red. (Pre-failure imagery: NAIP image; post-failure imagery: ArcGIS world imagery.)

5.5 ft (1.68 m) higher than normal operating levels (approximately 1.5 ft [0.46 m] below the crest elevation of the southeast embankment). The failure widened throughout the evening of May 19, and Wixom Lake was emptied. Figure 3 presents a pre- and post-failure comparison of the Edenville Dam. It was also reported that the downstream embankment slope was not uniform and was over-steepened in areas, and a bulging feature

Table 1. *Parameters used for processing interferometric synthetic aperture radar (InSAR) time-series analysis.*

Parameter	Value	Parameter	Value
weed_standard_dev (rad)	1.2	unwrap_time_win	180
unwrap_method	3D	unwrap_grid_size	10
scla_deramp	'y'	scn_time_win	180
scn_wavelength	50		

was present in a 2017 light detection and ranging (LiDAR) survey. A slope stability model showed a low factor of safety (1.08) for a rotational slide when modeled with the reservoir level at the time of failure.

MATERIALS AND METHODS

InSAR Analysis

The deformation of the earthen embankment of the Edenville Dam was investigated using Sentinel-1 SAR data. The Sentinel-1 mission of the European Space Agency (ESA) includes a constellation of two polar-orbiting satellites utilizing C-band SAR imaging. In total, 97 single-look complex (SLC) SAR scenes in interferometric wide (IW) swath mode and from ascending orbits were acquired between December 2, 2016, and May 3, 2020, from the ESA. The complex value of SLC scenes can be interpreted as phase and amplitude components, in which the phase presents the ranging distance from the SAR sensor to the ground, and the amplitude suggests the backscattering after the electromagnetic waves interact with the ground surface. Ground deformation can be measured by computing the phase difference, i.e., ranging distance difference. Sentinel-1 scenes obtained during the winter season were excluded due to snow cover and thus volumetric decorrelation of SAR signals. Following the co-registration and resampling of all the SAR scenes to a given reference scene (acquisition on November 22, 2018, in this study), interferograms were generated by conjugate multiplication of selected two complex-format SAR scenes. The amplitude dispersion index (ADI) (Ferretti et al., 2001) was set to be ≤ 0.7 to sort out the PS target with comparatively stable amplitude spanning the time, e.g., man-made structures and rocks (Table 1).

Long-wavelength phase noise represented as a phase ramp was estimated and removed for each interferogram. The Statistical-Cost, Network-Flow Algorithm for Phase Unwrapping (SNAPHU) algorithm and a grid size of 10 m were applied to unwrap the interferometric phases (Chen and Zebker, 2001). The displacement phase was generated by removing phase artifacts due to topographic error, orbit error, and tropospheric delay. A moderate temporal window of 180 days was applied to filter out the temporally high frequency turbulent tropospheric delay during displacement inversion. Eventually, we derived spatiotemporal ground deformation at the location of PS targets through least-square estimations.

Soil Moisture Index (SMI)

The SMI is an index used to model the relative soil moisture content based on the dry and wet edges of the scatterplot between land surface temperature (LST) and normalized difference vegetation index (NDVI). The SMI values range from 0 to 1, with 0 representing relatively drier soil and 1 representing relatively wetter soil (Zhiming et al., 2004; Mallick et al., 2009; Parida et al., 2013; and Yuan et al., 2020). SMI was calculated as follows (Zhiming et al., 2004):

$$SMI = \frac{LST_{max} - LST}{LST_{max} - LST_{min}}, \quad (1)$$

where LST_{max} and LST_{min} are defined as

$$LST_{max} = a_1 \times NDVI + b_1, \quad (2)$$

$$LST_{min} = a_2 \times NDVI + b_2, \quad (3)$$

where a and b are the slope and intercept, respectively, of the dry and wet edges.

The boundary conditions of the LST-NDVI space are the dry and wet edges, or LST_{max} and LST_{min}, respectively. These bounding layers are the theoretical maximum and minimum of SMI values for the given scene and are linear. To model the dry and wet edges, linear regression was used. The NDVI and LST data corresponding to each scene were processed individually. To model the dry edge, the LST-NDVI plot was subset along the NDVI x axis to represent the boundary slopes for both the dry and wet edges. Within the subset, the LST/NDVI scatterplot was divided into bins of width 0.01 along the NDVI axis. The mean of the 10 highest LST values within each bin was used to fit the linear regression model (Mallick et al., 2009; Parida et al., 2013; and Yuan et al., 2020). To model the wet edge, a horizontal line was fitted to the LST-NDVI scatterplot. For all scenes analyzed, the wet edge was nearly horizontal (slope < 0.01); therefore, the wet edge was modeled as a horizontal line with a slope of 0 (Mallick et al., 2009). Similar to modeling the dry edge, the five lowest LST values in each bin were recorded for modeling the wet edge. Further, the mean of the lowest LST values was fitted to the horizontal linear model. Values in the LST/NDVI space outside the dry and wet edges were reclassified to either dry or wet edges (LST_{min} or LST_{max}).

The U.S. Geological Survey (USGS) manages Landsat multi-sensor image archives that are restructured into a formal collection structure to ensure a uniform data quality standard. The Landsat Collection 2 represents the second

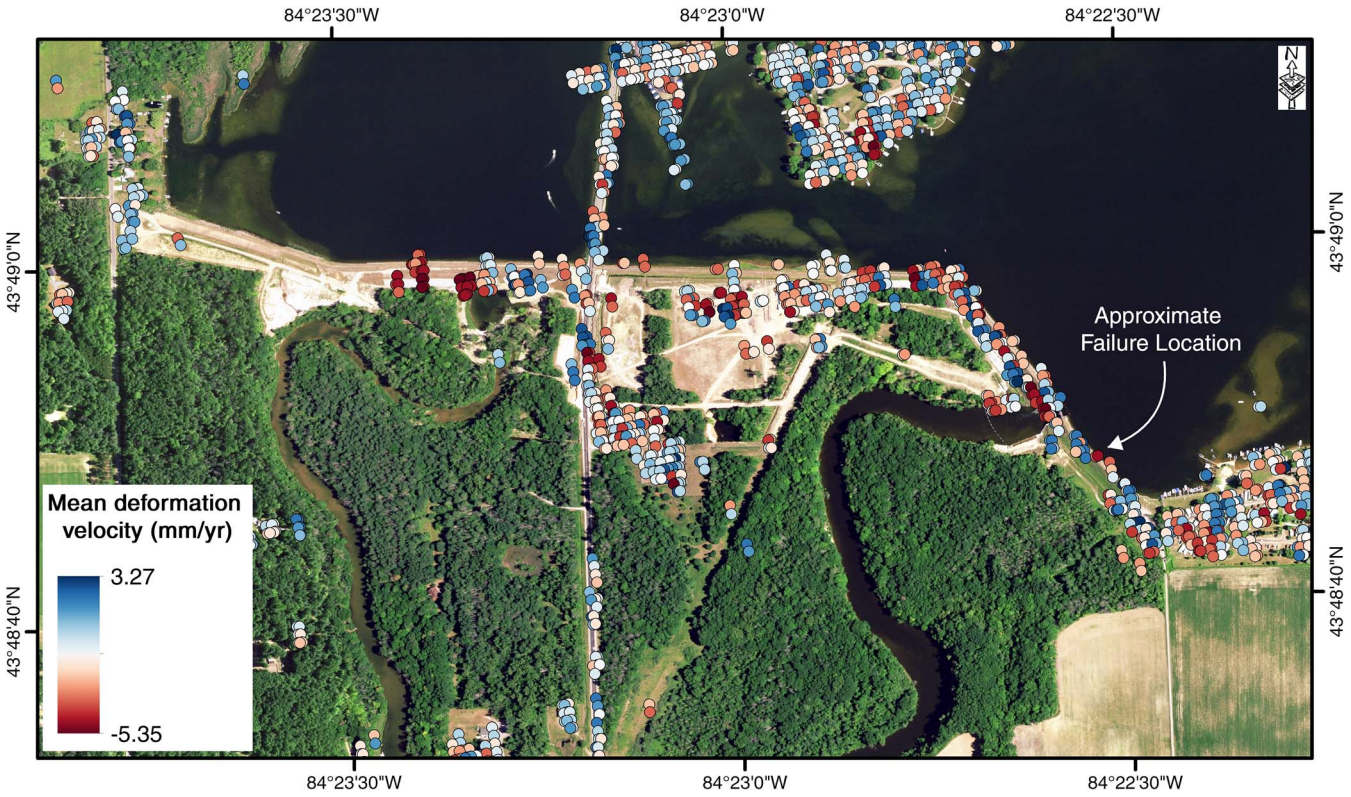

Figure 4 Average velocity (mm/yr) between December 2, 2016, and May 3, 2020, measured using 97 Sentinel-1 images with PSI processing.

significant update to this reprocessing effort, comprising calibrated, quantized, and scaled digital numbers with substantial improvements in absolute geolocation accuracy (Crawford et al., 2023). Fourteen Collection 2 Level 1 Landsat 8 images were obtained between April 23, 2016, and May 4, 2020, from the USGS Earth Explorer (https://earthexplorer.usgs.gov). Images between November and February were excluded due to snow cover and seasonal vegetation dormancy. Scenes with cloud cover within the specified extent were excluded from the analysis. The LST and NDVI layers were generated using the ERDAS IMAGINE software. The spatial resolution of Landsat data (multi-spectral Operational Land Imager [OLI] and resampled Thermal Infrared Sensor [TIRS] thermal bands) is 30 m; therefore, the spatial resolution of SMI is 30 m. A time series of the SMI was derived from the Landsat 8 images. A standard deviation map of the SMI time series was also derived to analyze the region's temporal variation of moisture content.

RESULTS

InSAR Analysis

The mean deformation velocity from the PSI measurements from December 2, 2016, to May 3, 2020, for the region, is shown in Figure 4. The mean deformation velocity of the region varied between −5.35 mm/yr and 3.27 mm/yr. The mean deformation velocity was measured in the line-of-sight (LOS) direction (approximately N80°E, 40° to nadir), where positive and negative values were PS targets moving toward (i.e., upward) and away (e.g., downward) from the satellite, respectively (Vassileva et al., 2017). Three areas of interest (AOIs) were identified to compare the movement along the dam outline: the west embankment, the east embankment, and the southeast embankment where the failure occurred. The three embankments included in the AOIs had a difference in elevation from the reservoir to the toe of the dam between 8 and 12 m. The southeast embankment containing the failure location begins immediately southeast of the Edenville Spillway and extends southeast to the easternmost abutment. The mean (standard deviation) deformation velocity for the PSI measurements of the west, east and southeast embankments were −1.1 mm/yr (1.8 mm/yr), −0.1 mm/yr (1.5 mm/yr), and −0.5 mm/yr (1.1 mm/yr), respectively (Table 2). This variability in InSAR resulted from the heavily vegetated floodplain environment and coarse spatial resolution relative to the narrow embankment system. The average cumulative displacements of the east, west, and southeast embankments showed no major differences and were −21.3 mm, −47.5

Table 2. *Summary of the persistent scatterer interferometry (PSI) analysis of the embankments of the Edenville Dam.*

	Southeast	East	West
Number of PS	44	116	57
PS density (per ha)	34	61	33
Average cumulative displacement (mm)	−33.2	−21.3	−47.5
Mean deformation velocity (mm/yr)	−0.5	−0.1	−1.1
Standard deviation of deformation velocity (mm/yr)	1.1	1.5	1.8
Maximum deformation velocity (mm/yr)	2.8	3.1	2.5
Minimum deformation velocity (mm/yr)	−2.3	−3.6	−5.4

mm, and −33.2 mm, respectively. Most PS targets in all three AOIs had deformation velocities that fell within two standard deviations. Although the southeast embankment is considered to represent an unstable area of the dam, as the failure occurred within this AOI, insufficient numbers of PS targets were resolved within the approximated failure location.

Soil Moisture Index (SMI)

The SMI representing relative moisture in the study area was derived from the Landsat 8 images between April 23, 2016, and May 4, 2020 (Figure 5). The standard deviation of the SMI time series is shown in Figure 6. The SMI scenes were not evenly distributed over time due to the lack of cloud-free images. Based on the standard deviation, the areas with the greatest variability in the entire scene were the agricultural fields shown in the southeast corner and the two "bull's-eye" features along the western edge of the scene, with values ranging from 0.20 to 0.30. The SMI values for the Edenville Dam ranged between 0.5 and 0.9. As expected, the highest SMI values were observed at or around Wixom Lake and the Tobacco and Tittabawassee Rivers, while the lowest SMI values were observed in the urban areas, the land area between the east and west sides of Wixom Lake, and the agricultural fields to the southeast of the Edenville Dam. Areas downstream of the southeast embankment also showed relatively lower temporal variability in the SMI. The SMI scenes in April and May appeared to have less contrast ("blurrier") between varying land-use types, i.e., urban, agricultural, forested, and water.

DISCUSSION

The results of the PSI analysis of the Edenville Dam did not provide any significant observations supporting the deformation of the southeast embankment and apparent displacement at the failure location over the period of study. Although the southeast embankment recorded a negative displacement, the magnitude was not significant (within two standard deviations) and was comparable with the east and west embankments, representing stable conditions. The lack of evidence of noticeable deformation of the southeast embankment highlights the limitations of InSAR techniques in vegetated floodplains or when the deformation magnitude is beyond the capabilities of the InSAR technique. Theoretically, the maximum relative deformation rate measurable for Sentinel-1 is tens of centimeters per year in a distance of one pixel spacing, but it varies with the noise level of the data and the specific phase unwrapping technique used to resolve phase ambiguities (Crosetto et al., 2016).

The SMI analysis for the Edenville Dam illustrates the variations in relative soil moisture content from April 2016 to May 2020. Consistent soil moisture conditions are to be expected in an earth dam structure constructed with engineered drainage. Relatively higher SMI values are anticipated in the areas near the dam and spillway, which is evident in Figure 6. However, a linear stretch of consistent saturation (or higher SMI values) trending southwest was observed in most of the images. The relatively lower standard deviation of this zone (Figure 6) implies consistent saturation of the zone, suggesting the possibility of perennial subsurface seepage. It is worth noting that the post-dam break river channel developed through this saturation zone. Hence, we argue that the saturated zone perpendicular to the embankment reflects the presence of a potential conduit mechanism for seepage and internal erosion for the embankment failure. Pradel et al. (2021) identified six terrace levels in the vicinity of the dam, where the second and third terrace levels pass beneath the dam at the approximate failure location and correspond to a change in elevation along the base of the dam (∼6.6 ft; ∼2.0 m) and a change in underlying geology. The association between different terrace treads and glacial stratigraphy implies that the embankment predominantly rests on glacial till of varying ages and physical characteristics. However, in certain areas, the sub-dam stratigraphy is likely composed of glacial outwash and fluvial sands. Since the dam was constructed across these terraces, resulting in lateral variations in the thickness of the embankment and geological substrates (Pradel et al., 2021), these differences in the terraces could likely have facilitated consistent seepage. As previously noted, Pradel et al. (2021)

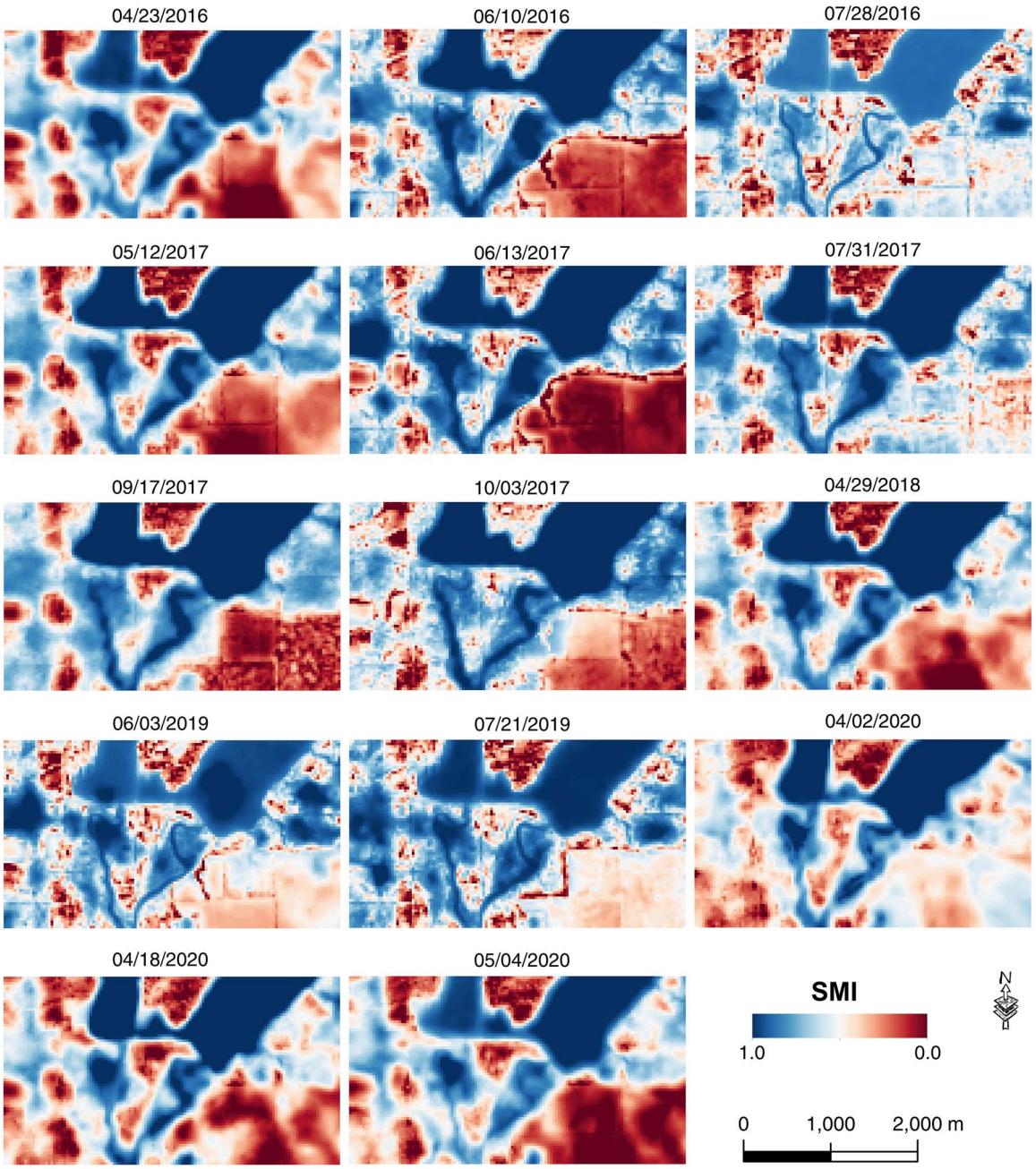

Figure 5. SMI time series for the 14 Landsat 8 images obtained between April 23, 2016, and May 4, 2020.

reported that the failed patch of the embankment corresponds to the topographic step between the second and third terrace surfaces. Based on the results of the InSAR and SMI analysis, we propose a model for the failure of the embankment. The southeast embankment had consistent subsurface seepage (zone of saturation) between the second and third terrace levels, reaching the Tittabawassee River roughly 750 m downstream of the Edenville Spillway. The elevated reservoir levels due to the storm event could have enhanced the pore-water pressure and seepage, forming a failure zone. The full reservoir level of the Wixom Lake also caused static liquefaction of earthen fill materials (Pradel et al., 2021), and these factors, in combination, facilitated a conventional rotational slope failure. The lack of evidence on the deformation of the embankment by the InSAR methods also reaffirms this hypothesis as static liquefaction occurs very quickly.

The operating rule curves for the reservoir (i.e., Wixom Lake) were to maintain water levels between +0.3 ft (0.09 m) and −0.4 ft (−0.12 m) of the normal pool level, except during floods and winter operations (France et al., 2022). Drawdown for the winter pool

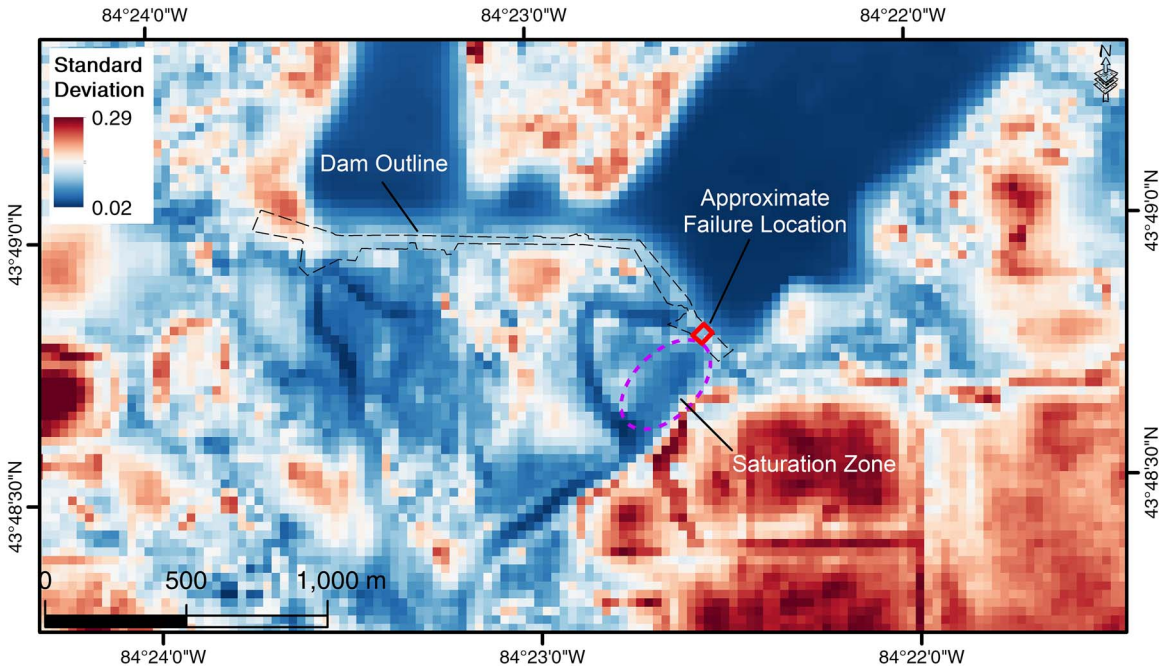

Figure 6. SMI standard deviation for the Edenville Dam area. The dam outline is shown as the black dashed portion. The approximate failure location is outlined in red.

level began after December 15 and lasted until January 15. Wixom Lake would return to normal pool level once surface temperatures reached 39°F (3.9°C). With consistent pool levels and adequate time when changing pool levels to avoid rapid drawdown, it is reasonable to assume that the phreatic surface would remain consistent throughout the year if proper drainage were installed. Rainfall could change the phreatic surface; however, properly engineered drainage would allow rainfall infiltration. The drainage system for the Edenville Dam consisted of clay tiles installed at the time of construction (Pradel et al., 2021; France et al., 2022). Original design drawings did not show the tiles; however, a 2012 survey of the dam's underdrain noted that the clay tiles were installed perpendicular to the face of the embankment, were uniformly spaced, and were discharged to a drainage ditch that ran parallel to the toe of the embankments. The survey also pointed out that along the southeast embankment, clay tiles were missing from the center of the approximate failure location, and some obstructions in the tiles were also observed (France et al., 2022). The lack of tiles could have resulted in a higher phreatic surface than in areas with greater clay tile density.

Although InSAR-based methods have been demonstrated to be precise and highly effective in monitoring the deformation of earthen embankment and dam failures (e.g., Grenerczy and Wegmüller, 2011; Gama et al., 2019; and Silva Rotta et al., 2020), the pre-dam failure analysis of the Edenville Dam using PSI did not offer any significant signs of movement across the southeast embankment. However, the SMI-based analysis facilitated the identification of potential failure zones with perennial seepage. Hence, this study undoubtedly suggests the requirement for a multi-sensor-based approach for periodic monitoring of dams. A major limitation of the SMI analysis is the lack of uniform temporal distribution due to cloud-covered scenes. Of the more than 50 Landsat 8 images obtained between April 2016 and May 2020 (excluding winter months), only 14 were able to be used in the analysis due to cloud cover. The coarse spatial resolution of the SMI data sets is another limitation of this study. The current advancements in drone-based multi-spectral imaging will provide a significant opportunity to overcome the limitations of the reliance on satellite-based SMI estimates. In the 2019 Brumadinho dam failure analysis (Silva Rotta et al., 2020), the spatial extent of the tailings dam was large enough that the use of 30 m satellite data was appropriate and could show variations in moisture content. Hence, a recommendation for future analysis of spatially small embankments is to use drone-based data sets, as ground sampling distances are much smaller, therefore allowing the observation of soil moisture variations in greater detail. A drone-based SMI analysis would also improve temporal uniformity as the drone can operate irrespective of the cloud cover.

SUMMARY AND CONCLUSION

In this study, we investigated the potential manifestations of the Edenville Dam failure (Michigan, midwestern United States) on May 19, 2020, using both PSI and

SMI analyses. The pre-failure analysis of the southeast embankment of the dam using PSI provided no clear evidence of displacement anomalies. Further, the rate of deformation and cumulative displacement of the failed (southeast) embankment were comparable with the stable conditions (east and west embankments). The time-series analysis of the satellite-derived SMI highlighted the potential failure zone as a chronic subsurface seepage zone (zone of saturation) between the second and third terrace levels, which is supported by the post-failure channel development. Based on the results of the analysis, we proposed a model for the failure of the Edenville Dam: The elevated reservoir water level during the storm event might have caused static liquefaction of earthen fill materials and increased the pore-water pressure and seepage, potentially creating a zone of weakness, and these factors, in combination, likely led to a conventional rotational slope failure and failure of the embankment. Thus, this study highlights the significance of multi-sensor-based remote-sensing (multi-spectral, thermal, and radar) approaches in the periodic monitoring of critical infrastructure, such as dams.

ACKNOWLEDGMENTS

The first author acknowledges the partial support for this work from Michigan Space Grant Consortium (MSGC) Fellowship grant no. 80NSSC20M0124.

DISCLAIMER

The authors declare no conflict of interest.

REFERENCES

Besoya, M.; Govil, H.; and Bhaumik, P., 2020, A review on surface deformation evaluation using multitemporal SAR interferometry techniques: *Spatial Information Research*, Vol. 29, No. 3, pp. 267–280.

Chen, C. W. and Zebker, H. A., 2001, Two-dimensional phase unwrapping with use of statistical models for cost functions in nonlinear optimization: *Journal of the Optical Society of America A*, Vol. 18, No. 2, pp. 338–351.

Crawford, C. J.; Roy, D. P.; Arab, S.; Barnes, C.; Vermote, E.; Hulley, G.; Gerace, A.; Choate, M.; Engebretson, C.; Micijevic, E.; Schmidt, G.; Anderson, C.; Anderson, M.; Bouchard, M.; Cook, B.; Dittmeier, R.; Howard, D.; Jenkerson, C.; Kim, M.; Kleyians, T.; Maiersperger, T.; Mueller, C.; Neigh, C.; Owen, L.; Page, B.; Pahlevan, N.; Rengarajan, R.; Roger, J.-C.; Sayler, K.; Scaramuzza, P.; Skakun, S.; Yan, L.; Zhang, H. K.; Zhu, Z.; and Zahn, S., 2023, The 50-year Landsat Collection 2 archive: *Science of Remote Sensing*, Vol. 8, pp. 100103.

Crosetto, M.; Monserrat, O.; Cuevas-González, M.; Devanthéry, N.; and Crippa, B., 2016, Persistent Scatterer Interferometry—A review: *ISPRS Journal of Photogrammetry and Remote Sensing*, Vol. 115, pp. 78–89.

Dorr, J. A. and Eschman, D. F., 1970. *Geology of Michigan*: University of Michigan Press, Ann Arbor, MI, 488 p.

EGLE (Department of Environment, Great Lakes, and Energy), 2023, *Michigan Dam Inventory*: Electronic document, available at https://gis-egle.hub.arcgis.com/datasets/egle::michigan-dam-inventory/about

FEMA (Federal Emergency Management Agency), 2022, *Michigan Dam Incident Response Review—An Analysis of the 2020 Edenville and Sanford Dam Failure Response*: Electronic document, available at https://www.fema.gov/sites/default/files/documents/fema_michigan-dam-incident-response-review_report.pdf

Ferretti, A.; Fumagalli, A.; Novali, F.; Prati, C.; Rocca, F.; and Rucci, A., 2011, A new algorithm for processing interferometric data-stacks—SqueeSAR: *IEEE Transactions on Geoscience and Remote Sensing*, Vol. 49, No. 9, pp. 3460–3470.

Ferretti, A.; Prati, C.; and Rocca, F., 2001, Permanent scatterers in SAR interferometry: *IEEE Transactions on Geoscience and Remote Sensing*, Vol. 39, No. 1, pp. 8–20.

Foster, M.; Fell, R.; and Spannagle, M., 2000. The statistics of embankment dam failures and accidents: *Canadian Geotechnical Journal*, Vol. 37, No. 5, pp. 1000–1024.

France, J. W.; Alvi, I. A.; Miller, A. C.; Williams, J. L.; and Higinbotham, S., 2022, *Investigation of Failures of Edenville and Sanford Dams*: Federal Energy Regulatory Commission. Electronic document, available at https://damsafety-prod.s3.amazonaws.com/s3fs-public/files/Edenville-Sanford_Final%20Report_Main%20Report%20and%20Appendices.pdf

Gama, F. F.; Paradella, W. R.; Mura, J. C.; and De Oliveira, C. G., 2019, Advanced DINSAR analysis on dam stability monitoring—A case study in the Germano mining complex (Mariana, Brazil) with SBAS and PSI techniques: *Remote Sensing Applications: Society and Environment*, Vol. 16, pp. 100267.

Graham, W. J., 2009, Major U.S. dam failures—Their cause, resultant losses, and impact on dam safety programs and engineering practice. In Rogers, J. R. (Editor), *Great Rivers History: Proceedings and Invited Papers for the EWRI Congress and History Symposium*: American Society of Civil Engineers, Kansas City, MO, pp. 52–60.

Grenerczy, G. and Wegmüller, U., 2011, Persistent scatterer interferometry analysis of the embankment failure of a red mud reservoir using ENVISAT ASAR data: *Natural Hazards*, Vol. 59, No. 2, pp. 1047–1053.

Kehew, A. E.; Esch, J. M.; Kozlowski, A. L.; and Ewald, S. K., 2012, Glacial land systems and dynamics of the Saginaw Lobe of the Laurentide Ice Sheet, Michigan, USA: *Quaternary International*, Vol. 260, pp. 21–31.

Larson, G. and Schaetzl, R., 2001, Origin and evolution of the Great Lakes: *Journal of Great Lakes Research*, Vol. 27, No. 4, pp. 518–546.

Lin, Y. N.; Park, E.; Wang, Y.; Quek, Y. P.; Lim, J.; Alcantara, E.; and Loc, H. H., 2021, The 2020 Hpakant Jade mine disaster, Myanmar—A multi-sensor investigation for slope failure: *ISPRS Journal of Photogrammetry and Remote Sensing*, Vol. 177, pp. 291–305.

Mallick, K.; Bhattacharya, B. K.; and Patel, N. K., 2009. Estimating volumetric surface moisture content for cropped soils using a soil wetness index based on surface temperature and NDVI: *Agricultural and Forest Meteorology*, Vol. 149, No. 8, pp. 1327–1342.

Maltese, A.; Pipitone, C.; Dardanelli, G.; Capodici, F.; and Muller, J.-P., 2021, Toward a comprehensive dam monitoring—On-site and remote-retrieved forcing factors and resulting displacements (GNSS and PS-InSAR): *Remote Sensing*, Vol. 13, No. 8, pp. 1543.

Michigan Section of the American Society of Civil Engineers, 2023, *2023 Report Card for Michigan's Infrastructure*: American Society of Civil Engineers. Electronic document, available at https://infrastructurereportcard.org/wp-content/uploads/2016/10/Report-2023-MI-IRC-Final-WEB.pdf

Mura, J.; Gama, F.; Paradella, W.; Negrão, P.; Carneiro, S.; De Oliveira, C.; and Brandão, W., 2018, Monitoring the vulnerability of the dam and dikes in Germano iron mining area after the collapse of the tailings dam of Fundão (Mariana-MG, Brazil) using DInSAR techniques with TerraSAR-X data: *Remote Sensing*, Vol. 10, No. 10, pp. 1507.

National Performance of Dams Program, 2018, *Dam Failures in the U.S.*: Department of Civil & Environmental Engineering, Stanford University. Electronic document, available at https://npdp.stanford.edu/sites/default/files/reports/npdp_dam_failure_summary_compilation_v1_2018.pdf

Othman, A. A.; Al-Maamar, A. F.; Al-Manmi, D. A. M.; Liesenberg, V.; Hasan, S. E.; Al-Saady, Y. I.; Shihab, A. T.; and Khwedim, K., 2019, Application of DInSAR-PSI technology for deformation monitoring of the Mosul Dam, Iraq: *Remote Sensing*, Vol. 11, No. 22, pp. 2632.

Parida, B. R.; Collado, W. B.; Borah, R.; Hazarika, M. K.; and Samarakoon, L., 2013, Detecting drought-prone areas of rice agriculture using a MODIS-derived soil moisture index: *GIScience & Remote Sensing*, Vol. 45, No. 1, pp. 109–129.

Pradel, D.; Lobbestael, A.; Athanasopoulos-Zekkos, A.; Brooks, C.; Champagne, C.; Clark, M.; Dobson, R.; Edmonds, D.; Esser, A.; Gong, W.; Hille, M.; Manousakis, J.; Marion, N.; Martin, H.; Midttun, N.; Niemi, N.; Oommen, T.; Townsend, K.; Yanites, B.; and Zekkos, D., 2021, *Edenville and Sanford Dam Failures: Field Reconnaissance Report*: American Society of Civil Engineers, Reston, VA.

Redlinger, J. F.; Copen, M. D.; Judd, W. R.; Matthews, J. S.; Perdue, J. M., Jr.; Sherlock, P.; Vithalani, J.; Wahler, W. A.; and Wilson, G. R., 1975, *Lessons from Dam Incidents USA*: American Society of Civil Engineers, New York, NY.

Silva Rotta, L. H.; Alcântara, E.; Park, E.; Negri, R. G.; Lin, Y. N.; Bernardo, N.; Mendes, T. S. G.; and Souza Filho, C. R., 2020, The 2019 Brumadinho tailings dam collapse: Possible cause and impacts of the worst human and environmental disaster in Brazil: *International Journal of Applied Earth Observation and Geoinformation*, Vol. 90, pp. 102119.

Vassileva, M.; Giulio Tonolo, F.; Riccardi, P.; Lecci, D.; Boccardo, P.; and Chiesa, G., 2017, Satellite SAR interferometric techniques in support to emergency mapping: *European Journal of Remote Sensing*, Vol. 50, No. 1, pp. 464–477.

Wu, W. M.; Altinakar, M. S.; Al-Riffai, M.; Bergman, N.; Bradford, S. F.; Cao, Z. X.; Chen, Q. J.; Constantinescu, S. G.; Duan, J. G.; Gee, D. M.; Greimann, B.; Hanson, G.; He, Z. G.; Hegedus, P.; Van Hoestenberghe, T.; Huddleston, D.; Hughes, S. A.; Imran, J.; Jia, Y. F.; Jorgeson, J. D.; Kahawita, R.; Klumpp, C. C.; Lai, Y.; Langendoen, E. J.; Liu, S. E. L.; Moreda, F.; Morris, M.; Morvan, H.; Orendorff, B.; Pak, J.; Peeters, P.; Reed, S.; Sanders, B. F.; Scott, S. H.; Soares-Frazao, S.; Song, C. R.; Sutherland, J.; Teal, M. J.; Tsubaki, R.; Wahl, T. L.; Weston, D. M.; Williams, D. T.; Zech, Y.; Zhang, L. M.; and ASCE EWRI Task Committee on Dam/Levee Breaching, 2011, Earthen Embankment Breaching: *Journal of Hydraulic Engineering*, Vol. 137, No. 12, pp. 1549–1564.

Yuan, L.; Li, L.; Zhang, T.; Chen, L.; Zhao, J.; Hu, S.; Cheng, L.; and Liu, W., 2020, Soil moisture estimation for the Chinese Loess Plateau using MODIS-derived ATI and TVDI: *Remote Sensing*, Vol. 12, No. 18, pp. 3040.

Zhang, Z.; Wang, C.; Tang, Y.; Fu, Q.; and Zhang, H., 2015, Subsidence monitoring in coal area using time-series InSAR combining persistent scatterers and distributed scatterers: *International Journal of Applied Earth Observation and Geoinformation*, Vol. 39, pp. 49–55.

Zhiming, Z.; Qiming, Q.; and Xin, W., 2004, The application of LST/NDVI index for monitoring land surface moisture in semiarid area. In *IGARSS 2004: 2004 IEEE International Geoscience and Remote Sensing Symposium*, Vol. 7: The Institute of Electrical and Electronics Engineers, Piscataway, NJ, pp. 1551–1554.

Zumr, D.; David, V.; Jeřábek, J.; Noreika, N.; and Krása, J., 2020, Monitoring of the soil moisture regime of an earth-filled dam by means of electrical resistance tomography, close range photogrammetry, and thermal imaging: *Environmental Earth Sciences*, Vol. 79, No. 12, pp. 299.